IEEE Access
Multidisciplinary | Rapid Review | Open Access Journal

Received 1 September 2023, accepted 23 September 2023, date of publication 2 October 2023, date of current version 9 October 2023.

Digital Object Identifier 10.1109/ACCESS.2023.3321348

RESEARCH ARTICLE

Wideband/Wide-Angle Planar Single-Layer Retroreflector Using Double Gradient Metasurfaces

ALI PESARAKLOO AND MOHAMMAD KHALAJ-AMIRHOSSEINI
Department of Electrical Engineering, Iran University of Science and Technology, Tehran 13114-16846, Iran
Corresponding author: Ali Pesarakloo (ali_pesarakloo@elec.iust.ac.ir)

ABSTRACT In this paper, a new type of metasurface called Double Gradient Metasurface (DGM) is proposed, which can be used to implement a planar and low-profile retroreflector with a continuous wide incident angle range or a wide frequency width. The proposed structure consists of a set of supercells with a number of unitcells embedded into them. The design is performed based on the array factor method, taking into account the periodicity gradient of supercells and the phase gradient of unitcells. To validate the proposed method, two retroreflector prototypes with a thickness approximately equal to $0.04\lambda_o$ are designed and fabricated. The first prototype is designed for a continuous wide incident angle view from 15° to 50° at 10 GHz. The second prototype is designed for a wide frequency range from 9GHz to 11 GHz at an incident angle of 20°.

INDEX TERMS Electromagnetic metasurface, planar retroreflector, array theory.

I. INTRODUCTION

Metasurfaces are periodic or aperiodic structures with subwavelength thickness composed of subwavelength scatterers [1], [2], [3]. In periodic metasurfaces, the dimensions of the lattices are equal to each other, as well as the geometric parameters of the scatterers. Howevere, in aperiodic metasurfaces, the geometric parameters of the scatterers differ from each other [4]. Metasurfaces are used to control the scattering of electromagnetic waves impinging on the structure. Over recent years, various functionalities of metasurfaces have been proposed, including anomalous reflection and refraction, polarization conversion, absorption, flat lens, cloaking, holography, spatial filtering, analog computing, and more [1]. To design a metasurface with a specific functionality, various modeling techniques have been proposed in the literature, such as reflection and transmission phase, surface impedances and admittances, effective polarizabilities, effective susceptibilities, and equivalent circuits [1], [2].

One of the functionalities of metasurfaces that has gained a lot of interest recently is retroreflection. Retroreflectivity is defined as the ability to reflect an incident signal in the same direction from which it originated, without any prior knowledge of the arrival direction [5]. Retroreflection plays important role in various fields, including navigation safety, maritime distress rescue, vehicle collision avoidance systems in the civil sector, as well as radar calibration, stealth, and deception in the military sector [6], [7], [8].

To the best of our knowledge, the first metasurface with retroreflection property in microwave frequencies was achieved by Doumanis et al. in 2013. They designed a flat surface to reflect a TE polarized wave incident at 45° back in the direction of the impinging signal at 14.7 GHz, based on a combination of Floquet theory and the reflect-array principle [9]. Jia et al. designed a phase gradient metasurface following the generalized Snell's law, which can retroreflect incident waves with an angle of $\theta_i = 20°$ backward at 9.8GHz under transverse electric (TE) polarizations [10]. Wong et al. designed, simulated, and measured two binary Huygens' metasurfaces at a frequency of 24 GHz, which retroreflect an incident plane wave at 82.87° from broadside for TE and TM polarized waves, respectively. The measured results show a power efficiency of 93% for both TE and TM polarizations [11]. Hoang et al. presented three types of two-dimensional

The associate editor coordinating the review of this manuscript and approving it for publication was Wanchen Yang.

retrodirective phase gradient metasurfaces corresponding to the three retrodirected angles of $-20°$, $-30°$, and $-40°$, respectively, with a power efficiency of more than 94% in both directions. Furthermore, the fractional 3-dB bandwidths of the retroreflections are improved up to 12% by increasing the air gap of the substrate from the ground plane by about $\lambda_0/4$ [5]. In 2020, Tao et al. proposed non-periodic metasurfaces used for retroreflection in one oblique incident wave with linear polarization (TE/TM) and circular polarization (CP). The proposed metasurfaces consist of non-periodic group cells (the lattice period of group cells is equal to each other, but the geometric parameters of the scatterers are different), optimized by genetic algorithm for desired scattered power patterns [4].

In all of the works mentioned so far, the metasurfaces were designed only for a single incident angle, and the response for waves incident from other directions was not engineered. To achieve multi-angle retroreflectivity, Asadchy et al. proposed three- and five-channel retroreflector based on the surface impedance model with a periodicity of $\lambda < P < 2\lambda$. For the designed and optimized three-channel retroreflector, the incident angles are directed at $-70°$, $0°$, and $70°$, with a minimum achievable efficiency of 92.8% [12]. Feng et al. proposed a structure based on the multiple phase gradient modulated metasurface. In this structure, the surface is decomposed into several regions with different areas, each designed for one incident angle following the phase gradient metasurface [8]. Another method to achieve multi-angle retroreflectivity is to use a metasurface with high super-cell periodicities greater than 2λ, as proposed by Kalaagi et al. [15]. They designed a retrodirective metasurface following the generalized phase law of reflection and the surface impedance modulation technique with a supercell periodicity of 2.88λ at 14.7 GHz. Retroreflection has been achieved at eleven angles simultaneously [13]. Memarian et al. presented a retroreflective surface based on multiple coupled blazing resonances per cell, enabling retroreflectivity at multiple wavelengths, each corresponding to different incident wavenumbers [14]. The first work on retroreflectivity in a continuous angle range using planar metasurfaces was done in 2017 by Arbabi et al. [15]. They proposed a planar monolithic near-infrared retroreflector composed of two layers of silicon nanoposts, which, following the cat's eye theory, reflects light along its incident direction with a normal incidence efficiency of 78% and a large half-power field of view of $60°$. Then this method was subsequently implemented in the field of acoustics [16] and microwave [17], [18], [19].

From the works conducted so far in the field of retroreflectivity using metasurfaces, it can be concluded that single-layer metasurfaces with low thickness have only been utilized for single-angle or discrete multiple-angle retroreflection. Retroreflection in a continuous angular range has been achieved by employing two cascaded metasurfaces, resulting in a structure with a thickness of several wavelengths. In this paper, a novel configuration is proposed for the first time, consisting of a single-layer metasurface capable of achieving retroreflection with a continuous wide incident angle range (at one frequency) or a wide frequency width (at one incident angle). The proposed metasurface comprises two nested arrays: one is an array of supercells with a periodicity gradient property, and the other is an array of unitcells embedded into supercells with a phase gradient property. Hence, this metasurface is referred to as the Double Gradient Metasurface (DGM). The periodicity values of the supercells are designed based on the first negative order Floquet-Bloch mode in the Floquet theory, enabling coverage of a continuous incident angle range with a specified angular step. The dimensions of the unitcells in each supercell are designed and optimized using array theory to maximize the reflected power along the incident direction.

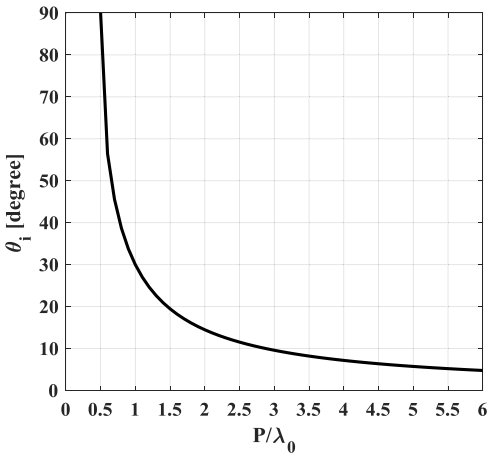

FIGURE 1. The diagram of the incident angle corresponding to the first negative Floquet mode against the periodicity of a periodic structure at frequency of 10 GHz.

II. THEORETICAL BACKGROUND

According to Floquet's theory, it is known that every periodic structure with a period greater than half a wavelength exhibits retroreflectivity properties at specific incident angles. These incident angles correspond to negative Floquet modes and their number depends on the periodicity of the structure. The relationship between the incident angle, mode number, and periodicity can be derived as follows [20]:

$$\theta_{retro,m} = \sin^{-1}\left(\frac{-m\lambda_0}{2P}\right) \tag{1}$$

where $\theta_{retro,m}$ is the incident angle for which the mth Floquet mode has retroreflectivity property, λ_0 is the wavelength corresponding to the frequency of the incident wave, and P is the periodicity of the periodic structure.

The first negative Floquet mode has maximum retroreflected power, so (1) becomes as follows:

$$\frac{P}{\lambda_0} = \frac{1}{2\sin(\theta_{retro})} \tag{2}$$

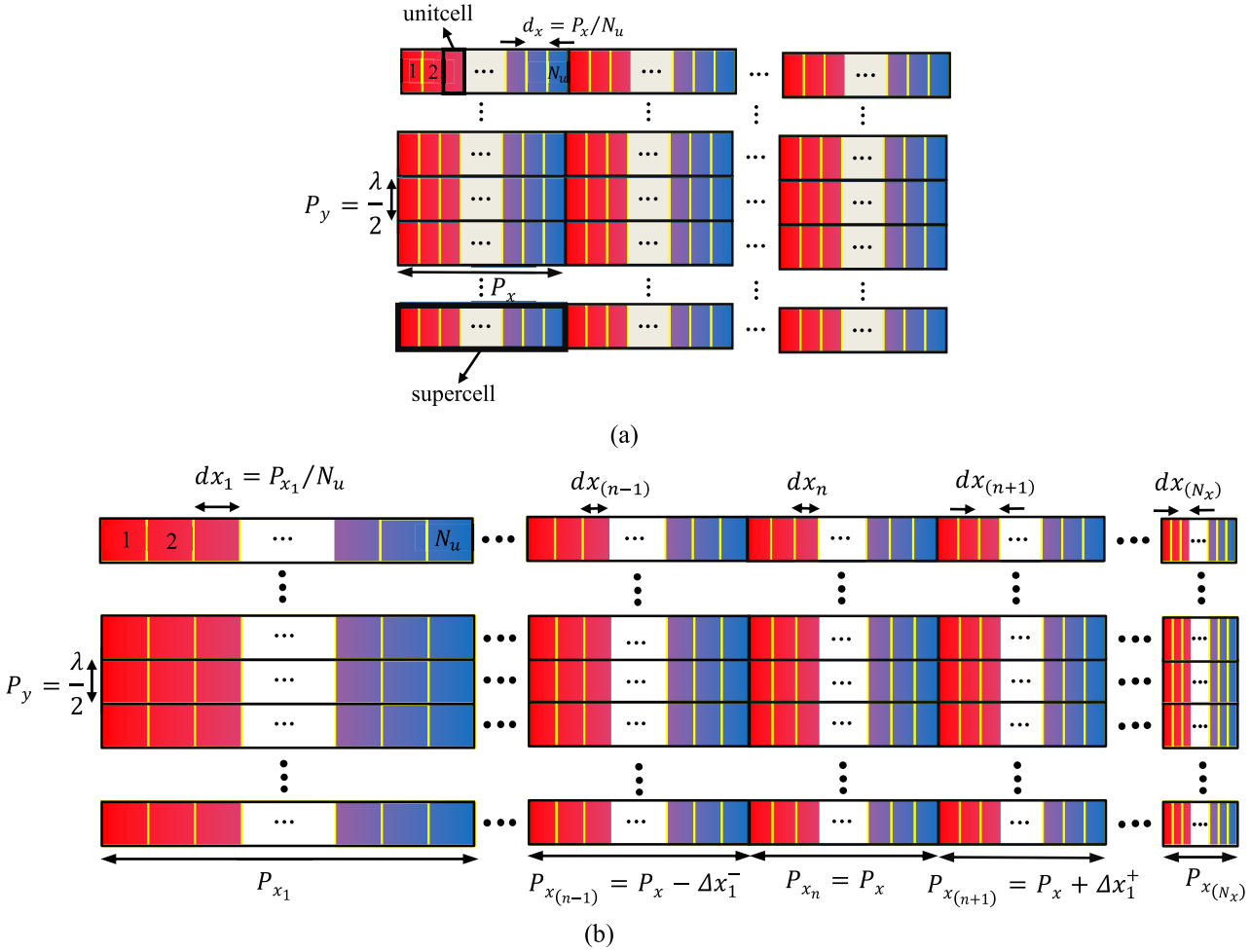

FIGURE 2. (a) An array of the supercell with periodicity P_x in which an array of unitcells is embedded, (b) An array of several supercells with different dimensions along horizontal direction that vary gradually.

The diagram related to (2), for a fixed frequency of 10 GHz, is depicted in Fig. 1.

As observed, with an increase in the ratio P/λ_0, the first negative Floquet mode manifests at a smaller incident angle.

To attain retroreflectivity across a wide continuous angular range using a flat and single-layer structure, it is proposed, based on Figure 1, to arrange multiple supercells with varying periods in a gradual manner. This proposition is supported by the notion that each supercell, along with its neighboring supercells, forms a quasi-periodic structure, which exhibits retroreflectivity at the corresponding incident angle of that particular supercell.

To further illustrate this concept, let's consider two arrays. The first array is a finite array ($N_x \times N_y$) consisting of a supercell with a periodicity P_x along the horizontal direction and a periodicity P_y along the vertical direction. According to Eq. 1, this array exhibits retroreflectivity at the incident angle of $\theta_{retro} = \sin^{-1}\left(\frac{\lambda_0}{2P_x}\right)$. The second array is also a finite array ($N_x \times N_y$), but it consists of several supercells with varying dimensions along the horizontal direction, gradually changing from one supercell to the next. In the center of the array, the supercell with a dimension of P_x is placed, resulting in longitudinal dimensions of the supercells as $\ldots, P_x - \Delta x_2^-, P_x - \Delta x_1^-, P_x, P_x + \Delta x_1^+, P_x + \Delta x_2^+, \ldots$. The periodicity along the vertical direction remains P_y. To achieve maximum power retroreflection at each incident angle, the unit cells embedded within each supercell are designed based on the phase gradients. Fig. 2 depicts these two types of arrays for better visualization.

To analyze these arrays, the array factor theory is employed. When a plane wave is incident on the array from a direction defined by (θ_i, φ_i), each unit cell experiences a different phase excitation due to the spatial phase delay caused by the incoming plane wave. Additionally, each unit cell reflects the wave with a specific phase determined by the dimensions of its patch. If the objective is to maximize radiation from the array in the direction specified by (θ_r, φ_r), the array factor for these two arrays can be derived as (3) and (4), shown at the bottom of the next page.

In the given equations, N_u represents the number of unitcells embedded in each supercell, which remains constant for all supercells. $[I_1, \ldots, I_{N_u}]$ and $[\phi_1, \ldots, \phi_{N_u}]$ denote the

amplitude and phase of the reflection coefficient of the unit-cells, respectively. Furthermore, $u = \sin\theta_r\cos\varphi_r + \sin\theta_i\cos\varphi_i$ and $v = \sin\theta_r\sin\varphi_r + \sin\theta_i\sin\varphi_i$.

Now, to derive the results, we consider $N_x = 7$, $N_y = 5$, $N_u = 8$, $P_x = 30$ mm, $P_y = 15$ mm. In this case, $\theta_{retro} = 30°$. The length of the supercells in array type 2 is determined using Fig. 1 with an angular step of 2.5°. The normalized monostatic RCS of both arrays is calculated using the array factor and plotted in Fig. 3. The results show that array type 1 exhibits maximum retroreflectivity at an incident angle of 30°. However, its retroreflectivity sharply degrades at adjacent angles. On the other hand, array type 2 achieves the maximum retroreflectivity at an incident angle of 28.5°, which is slightly shifted and lower than that of array type 1. However, array type 2 covers the adjacent angles more effectively. It is important to note that the assigned phases to the unitcells, obtained from the phase gradient method, are optimized for array type 1. These phases are not necessarily optimal for array type 2. By optimizing the phases specifically for array type 2, even better results can be achieved. However, for the purpose of comparison between the two arrays, the optimization process was not pursued. In the design section the optimization process for the phases is explained in detail.

In conclusion, when multiple supercells with gradually changing periods are assembled, and an array of unit cells with a phase gradient is embedded within them, the resulting structure realizes a wide-angle retroreflector. Although the maximum retroreflectivity is reduced, the angular range with retroreflectivity is extended. This proposed retroreflector, consisting of two nested arrays with gradient properties, namely an array of supercells with periodicity gradient and an array of unit cells with phase gradient, is referred to as the ''Double Gradient Metasurface (DGM)''.

In addition to its application as a wide-angle retroreflector, the proposed metasurface can also be utilized to achieve

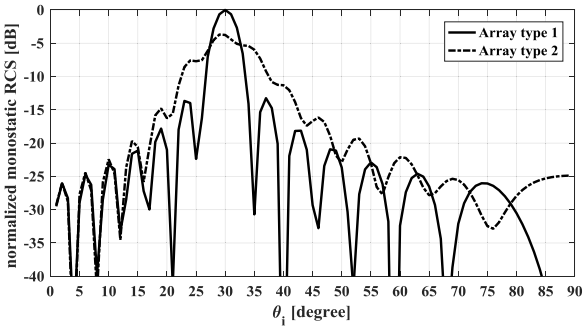

FIGURE 3. The normalized monostatic RCS diagram of the two arrays shown in Figure 2 in which the length of the supercells in array type 2 is selected for the angular step of 2.5°.

wideband retroreflection. In this case, (2) is employed for a fixed incident angle. Fig. 4 illustrates the diagram associated with (2) for fixed incident angles of $\theta_i = 20°$, 30°, and 40°. It can be observed that as the periodicity (P) decreases, the first negative Floquet mode occurs at higher frequencies for a fixed incident angle. To validate the performance of the proposed retroreflector for wideband mode, the two arrays depicted in Fig. 2 are utilized once again, with the only difference being that the length of the supercells in array type 2 is selected based on Fig. 4, using a frequency step of 0.2 GHz. The normalized monostatic RCS of these two arrays is then calculated using the array factor and plotted in Fig. 5.

As can be seen, the array type 2 exhibits retroreflectivity over a wider frequency range compared to array type 1. Therefore, it can be concluded that the proposed DGM can also be used in wideband retroreflector.

When a plane wave is incident on the proposed retroreflector from a specific direction, the supercells other than the one designed to respond to that direction also interact with the electromagnetic field. In this case, a portion of

$$F = \frac{1}{N_u}\left\{\begin{array}{c} I_1 e^{j\phi_1}\left[\exp\left(jk\frac{dx}{2}u\right)\right] \\ +I_2 e^{j\phi_2}\left[\exp\left(jk\frac{3dx}{2}u\right)\right] \\ +I_3 e^{j\phi_3}\left[\exp\left(jk\frac{5dx}{2}u\right)\right] \\ +\cdots \\ +I_{N_u} e^{j\phi_{N_u}}\left[\exp\left(jk\frac{(2N_u-1)dx}{2}u\right)\right] \end{array}\right\} \times \frac{1}{N_x \times N_y}\sum_{m=0}^{N_x-1}\sum_{n=0}^{N_y-1}\exp\left(jkmP_x u + jknP_y v\right) \tag{3}$$

$$F = \frac{1}{N_x}\left\{\begin{array}{c} \frac{1}{N_u}\left\{I_1 e^{j\phi_1}\left[\exp\left(jk\frac{dx_1}{2}u\right)\right] + I_2 e^{j\phi_2}\left[\exp\left(jk\frac{3dx_1}{2}u\right)\right] + \cdots + I_{N_u} e^{j\phi_{N_u}}\left[\exp\left(jk\frac{(2N_u-1)dx_1}{2}u\right)\right]\right\} \\ +\frac{1}{N_u}\left\{I_1 e^{j\phi_1}\left[\exp\left(jk\frac{dx_2}{2}u\right)\right] + I_2 e^{j\phi_2}\left[\exp\left(jk\frac{3dx_2}{2}u\right)\right] + \cdots + I_{N_u} e^{j\phi_{N_u}}\left[\exp\left(jk\frac{(2N_u-1)dx_2}{2}u\right)\right]\right\} e^{jkP_{x_1}u} + \\ +\cdots + \\ \frac{1}{N_u}\left\{I_1 e^{j\phi_1}\left[\exp\left(jk\frac{dx_{(N_x)}}{2}u\right)\right] + I_2 e^{j\phi_2}\left[\exp\left(jk\frac{3dx_{(N_x)}}{2}u\right)\right] + + \cdots + I_{N_u} e^{j\phi_{N_u}}\left[\exp\left(jk\frac{15dx_{(N_x)}}{2}u\right)\right]\right\} e^{jk(P_{x_1}+P_{x_2}+\cdots+P_{x_{(N_x)}})u} \end{array}\right\} \tag{4}$$

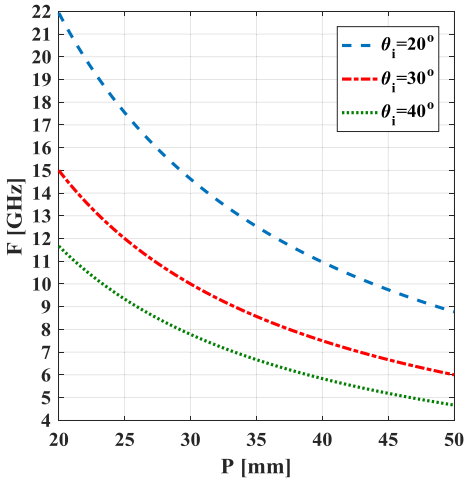

FIGURE 4. The diagram of the periodicity of a periodic structure against frequency for three different incident angle of the first negative Floquet mode.

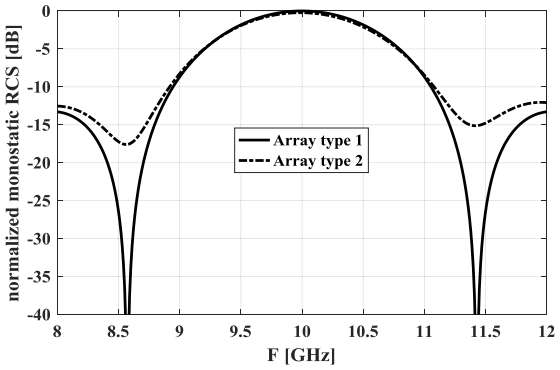

FIGURE 5. The normalized monostatic RCS diagram of the two arrays shown in Figure 2 in which the length of the supercells in array type 2 is selected for the frequency step of 0.2 GHz.

the retroreflector that includes the supercell designed for the given angle of incidence and the adjacent supercells actively participate in the retroreflection of the incident wave. Regarding the interaction of the other supercells with the electromagnetic field, the first negative Floquet mode, which is on the same side as the incident wave and exhibits the highest scattered power, is examined. The behavior of this mode is determined using the generalized Snell's reflection law, which can be expressed as follows:

$$\sin\theta_r = \sin\theta_i - \frac{\lambda_0}{P} \tag{5}$$

This equation is plotted in Fig. 6 for different incident angles and different supercell dimensions.

Indeed, as observed, supercells with different dimensions scatter the incident wave in directions other than the direction of incidence. Furthermore, as the dimensions of the supercells deviate further from those designed to respond to a specific incident angle, the angular directions of the scattered waves from these supercells also deviate further from the desired

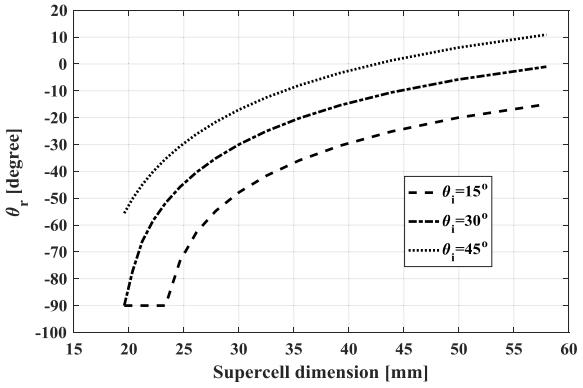

FIGURE 6. The diagram of the reflected angle against supercell dimensions for three different incident angle of the first negative Floquet mode.

incident angle. This deviation in angular directions prevents the occurrence of destructive interference between the wave scattered in the incident direction and the waves scattered by the other supercells. The same point can also be applied to the wideband retroreflector.

III. RETROREFLECTOR DESIGN

Now, we will explain the design process of the proposed retroreflector. Firstly, our focus is on the wide-angle retroreflector. The initial step in the design is to determine the dimensions of the different supercells that will be assembled together. This must be done while keeping in mind the ultimate goal of achieving a high and nearly constant RCS with minimal variation over a continuous wide angular range. To achieve this objective, we investigate the effect of different supercell dimensions on both its monostatic RCS and the adjacent supercells. The larger the dimensions of a supercell, the greater its monostatic RCS at the corresponding incident angle. However, its monostatic RCS decreases drastically in the adjacent incident angles. This occurs because the larger the dimensions of the supercell relative to the wavelength (which, according to Fig. 1, corresponds to the smaller incident angle), the greater the number of scattered propagating modes [11]. On the other hand, the smaller the dimensions of a supercell relative to the wavelength (which, according to Fig. 1, corresponds to the larger incident angle), the smaller its monostatic RCS at the corresponding incident angle. Nevertheless, it decreases gradually in the adjacent incident angles. Therefore, in this case, each supercell cooperates in increasing the monostatic RCS of the adjacent supercells. To validate this concept, we consider two arrays of supercells for incident angles of 15° and 50° at a frequency of 10 GHz, as shown in Fig. 7(a), (b). To retroreflect the maximum power at each incident angle, the embedded unitcells inside each supercell are designed based on the phase gradients. The normalized monostatic RCS diagram of these two structures is obtained using array factor theory, as shown in Figure 7(c).

As observed, for the designed structure at 15°, the monostatic RCS experiences a sharp decrease in the adjacent angles

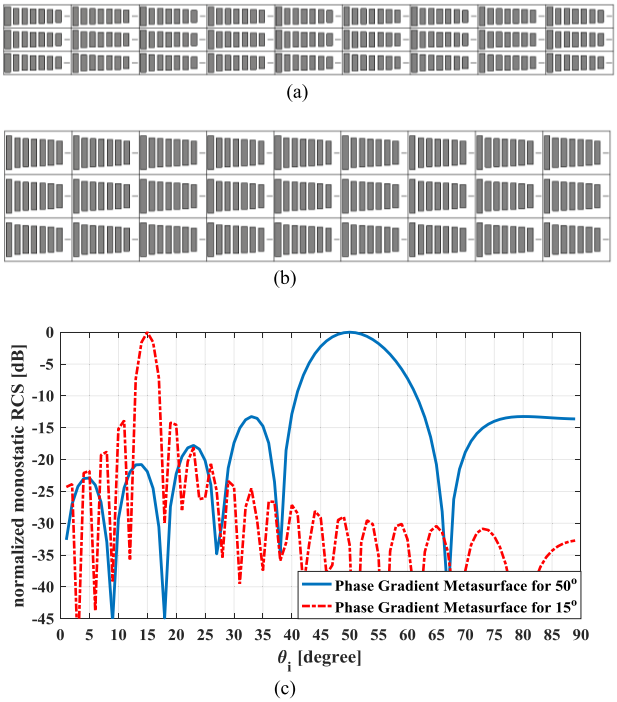

FIGURE 7. An array of supercells designed for the retroreflection in the incident angle of (a) 15°, (b) 50°, (c) the normalized monostatic RCS diagram of the structures (a) and (b).

to the designed angle. However, the opposite holds true for the designed structure at 50°.

Based on the aforementioned content, it can be inferred that in order to achieve a nearly constant RCS with minimal variation across the desired angular range, the periodicity of supercells with smaller dimensions should change gradually and slowly, while larger supercells should exhibit a faster rate of change. Fig. 1 illustrate that this condition is met when the dimensions of the supercells are selected based on a constant angular step. For the angular range of $10° \leq \theta_i \leq 50°$ with a step size of 2.5° and at a frequency of 10 GHz, the corresponding periodicity values are provided in Table 1.

The next step involves designing the structure embedded within each supercell to maximize retroreflected power in the corresponding incident angle, in both opposite directions. To accomplish this, an array of metallic strip unitcells is employed per supercell, as depicted in Fig. 8. It is evident that an air gap is incorporated within the unitcell. The rationale behind this choice is the utilization of an FR-4 substrate with high permittivity ($\varepsilon_r = 4.3$). Consequently, the unit cell designed with this substrate covers significantly less than a 360° reflection coefficient phase. Therefore, an air gap is introduced to decrease the overall dielectric coefficient. The optimal dimensions for the unit cell, which are consistent across all supercells, are as follows: $d_y = 15$ mm, $h_1 = 0.5$ mm and $h_2 = 0.75$ mm.

The next step involves determining the number of unitcells and their dimensions for each supercell. In order to ensure a

TABLE 1. The values of the periodicities correspond to the incident angle of the first negative Floquet mode in the angular range of $10° \leq \theta_i \leq 50°$ with the step of 2.5° and at the frequency of 10 GHz.

incident angle (θ_i) (degree)	10°	12.5°	15°	17.5°	20°	22.5°
Period (mm)	86.38	69.3	57.95	49.88	43.86	39.2
incident angle (θ_i) (degree)	25°	27.5°	30°	32.5°	35°	37.5°
Period (mm)	35.49	32.48	30	27.91	26.15	24.64
incident angle (θ_i) (degree)	40°	42.5°	45°	47.5°	50°	
Period (mm)	23.33	22.2	21.21	20.34	19.58	

TABLE 2. The values of the periodicities corresponding to the incident angle of the first negative Floquet mode for the frequency range of 9 GHz $\leq$ f $\leq$ 11 GHz with the step of 0.2 GHz and at the incident angle of 20°.

frequency (GHz)	9	9.2	9.4	9.6	9.8	10
Period (mm)	48.73	47.67	46.65	45.68	44.75	43.86
frequency (GHz)	10.2	10.4	10.6	10.8	11	
Period (mm)	43	42.18	41.37	40.61	39.87	

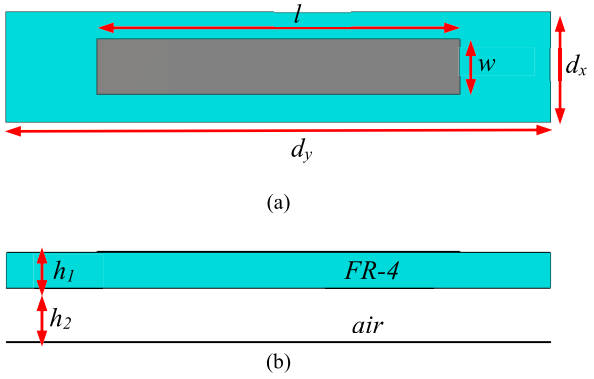

FIGURE 8. Geometry of the metallic strip unit cell (a) top view and (b) side view.

gradual variation in the unitcells placed within the supercells, the same number of unitcells is employed across all supercells. Consequently, the minimum number of unitcells is determined based on the largest supercell, ensuring that the dimensions of the unitcells are smaller than a quarter of the wavelength. In the case of the intended design at a frequency of 10 GHz and an angular range of $15° \leq \theta_i \leq 50°$ with a step size of 2.5°, the largest supercell, as indicated in Table 1, measures 57.95 mm. Therefore, a total of 8 unit cells are employed.

To determine the optimal dimensions of the unitcells within each supercell, we consider the array type 1 as shown in

TABLE 3. Comparison of the proposed retroreflector with the state-of-the-art works.

Ref.	elevation field of view	Max. ripple in RCS	directional property	Freq.	Thickness	minimum efficiency (%)
[15]	60°	3 dB	Not reported	353 THz	$588\lambda_0$	40
[17]	60°	3 dB	omnidirectional	10 GHz	$2.5\lambda_0$	23
[18]	60°	3 dB	omnidirectional	10 GHz	$3\lambda_0$	30
[19]	60°	3 dB	Not reported	10 GHz	$3\lambda_0$	18
[8]	50°	20 dB	Bi-directional	10 GHz	$0.1\lambda_0$	-
our work (wide-angle)	70°	4.3 dB	Bi-directional	10 GHz	$0.04\lambda_0$	12

Fig. 2(a), along with the array factor described by (3), where $N_u = 8$. In our desired scenario, where the plane wave is incident from the direction of the first negative Floquet mode and the reflected wave is in the same direction as the incidence, we have:

$$\begin{aligned} \sin(\theta_r) &= \sin(\theta_i) = \frac{\lambda}{2P_x} \\ \varphi_i &= \{0, \pi\} \\ \varphi_r &= \varphi_i + \pi \end{aligned} \tag{6}$$

In this case, the terms within the exponential function in (3) are obtained as follows:

$$\begin{aligned} & kmP_x \sin(\theta_r)\cos(\varphi_r) = kmP_x \sin(\theta_i)\cos(\varphi_i) \\ & = \frac{2\pi}{\lambda} mP_x \frac{\lambda}{2P_x} = m\pi \\ & \cdots\cdots\cdots\cdots\cdots\cdots\cdots\cdots \\ & 2k\frac{(2n-1)d_x}{2}\sin(\theta_r)\cos(\varphi_r) = 2k\frac{(2n-1)d_x}{2}\sin(\theta_i)\cos(\varphi_i) \\ & = 2\frac{2\pi}{\lambda}\frac{(2n-1)P_x}{2\times 8}\frac{\lambda}{2P_x} = \frac{(2n-1)\pi}{8} \end{aligned} \tag{7}$$

From (7), an important point can be extracted: the array factor of the structure in the retroreflection condition is independent of both the supercell periodicity and the operating frequency. In other words, if the optimal phase values of the unitcells $(\phi_1, \phi_2, \ldots, \phi_8)$ for a particular supercell and frequency are determined, these optimal values will hold true for supercells with different dimensions and at different frequencies.

The optimization of phase values and thus strip lengths of unitcells is carried out in two steps. Firstly, (3), along with (7), is optimized for a representative supercell to obtain the initial optimal phase values. These phases are then converted into initial strip lengths using the reflection phase versus strip length specific to each supercell's unitcell. Subsequently, an array of each supercell with the initial optimal strip length values of unitcells is simulated and further optimized using full-wave software to obtain the final optimal strip length values of unitcells. For the proposed retroreflector, it is desirable to achieve bidirectional functionality. This means that for each incident angle θ_i, the retroreflector should exhibit retroreflectivity in two opposite directions ($\varphi_i = 0^{\circ}, 180^{\circ}$). Therefore, during the optimization process, the phase of the unit cells is considered symmetrical with respect to the center of the supercell.

The optimal phase values of the unitcells, obtained by maximizing (3) along with (7), are:

$$\phi_1 = 37.9^{\circ}, \quad \phi_2 = 13.8^{\circ}, \ \phi_3 = -130.54^{\circ}, \ \phi_4 = -150^{\circ} \tag{8}$$

The design method for the proposed wideband retroreflector follows the previously mentioned design approach, with the difference that in this case, the supercell dimensions are obtained from (2) at a specific incident angle over a wide frequency range with a defined frequency step.

The specifications for the wideband retroreflector to be designed are as follows: a frequency range of 9 GHz $\leq f \leq$ 11 GHz with a step size of 0.2 GHz, and an incident angle of 20°. To achieve this, the periodicity values of the supercells are provided in Table 2. It is important to note that the optimal phase values of the unit cells mentioned in (8) also hold true for different frequencies. Therefore, the strip lengths corresponding to these phases are utilized as initial values in the optimization of the unitcells within each supercell using the full-wave software.

IV. SIMULATION AND MEASUREMENT

A. WIDE-ANGLE RETROREFLECTOR

The designed wide-angle retroreflector, intended for the angular range of $15^{\circ} \leq \theta_i \leq 50^{\circ}$ with steps of 10°, 5°,

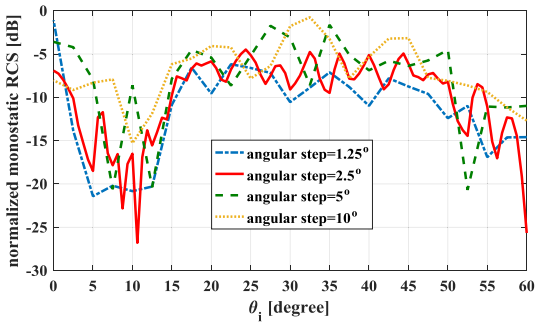

FIGURE 9. The normalized monostatic RCS of the simulated wide-angle retroreflector for the angular range of $15° \leq \theta_i \leq 50°$ with the steps of 10°, 5°, 2.5° and 1.25° at the frequency of 10 GHz.

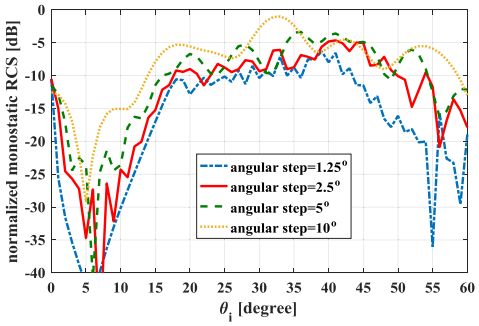

FIGURE 10. The normalized monostatic RCS diagram of the proposed wide-angle retroreflector for different angular steps obtained from the array factor.

2.5° and 1.25° at the a frequency of 10 GHz, has been simulated using CST STUDIO software. Based on Fig. 1, it is observed that as the incident angle approaches zero degrees, the supercell period and overall structure dimensions become very large. To avoid this issue, a non-zero incident angle is selected as the starting point in the angular range. The normalized monostatic RCS diagrams, obtained by calculating the difference between the monostatic RCS of the retroreflector and the specular reflection of a PEC structure with the same cross-section size, are depicted in Fig. 9.

To validate the results, they are also obtained using array type 2 as shown in Fig. 2(b), along with the array factor described by (4). Fig. 10 displays the normalized monostatic RCS diagram of the proposed retroreflector for various angular steps derived from the array factor.

Indeed, it can be observed that the overall variation pattern of the monostatic RCS in both Fig. 9 and Fig. 10 is similar. The minor differences between the two figures arise from the fact that the array factor method does not consider mutual coupling between unitcells. From Figs. 10 and 11, an important point can be extracted: the smaller the angular step, the less pronounced the ripple in the monostatic RCS. However, it is also noted that the average level of the monostatic RCS in the angular range of $15° \leq \theta_i \leq 50°$ decreases as the angular step decreases. Therefore, a compromise needs to be established when choosing the angular step, taking into consideration the maximum acceptable ripple and the average level of the monostatic RCS.

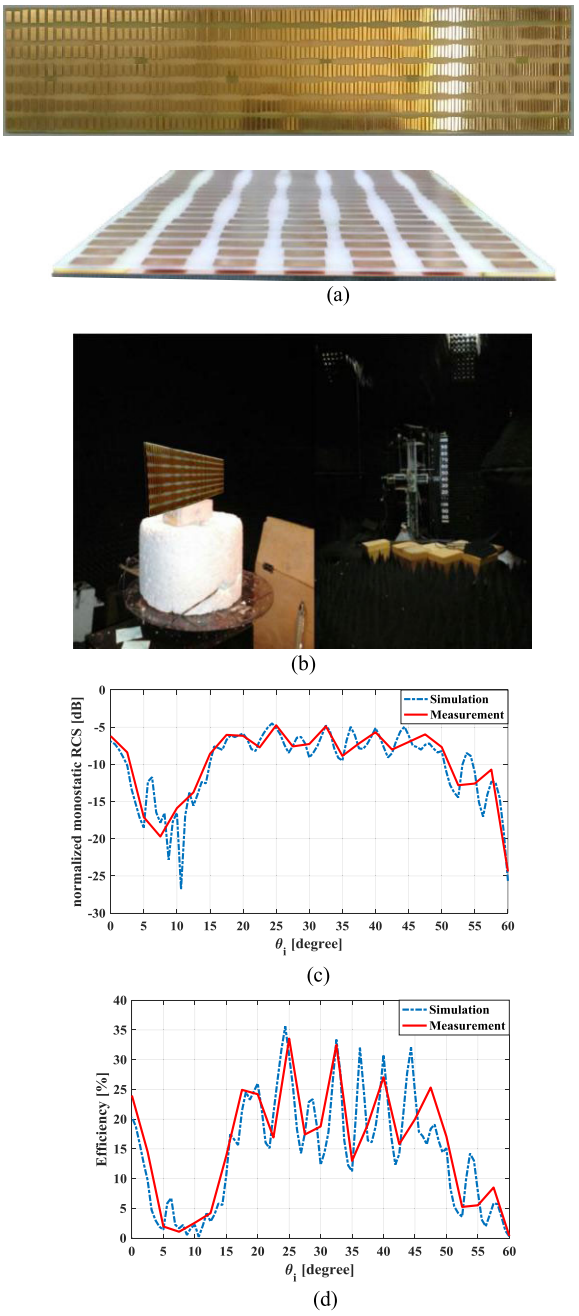

FIGURE 11. (a) The top and side view of the fabricated wide-angle retroreflector, (b) measurement setup, (c) and (d) Simulation and measurement results of the proposed retroreflector in the angular range of $15° \leq \theta_i \leq 50°$.

Here, the proposed retroreflector is fabricated for the angular step of 2.5°, as shown in Fig. 11(a). The overall dimension of the proposed wide-angle retroreflector is 45×350 mm^2. The measurement setup for monostatic RCS is exhibited in Fig. 11(b).

Fig. 11(c) presents the measured monostatic RCS of the manufactured structure at a frequency of 10 GHz, along with the corresponding simulation results.

It is evident that there is reasonable agreement between the measured and simulated monostatic RCS in the angular

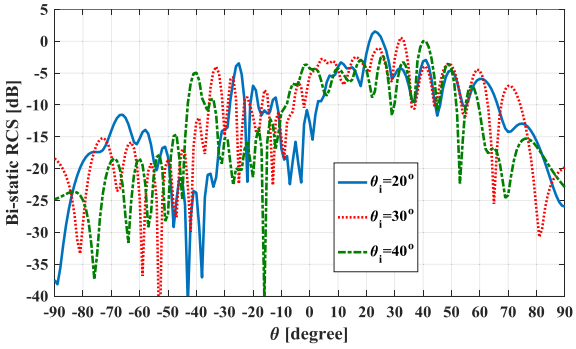

FIGURE 12. The bi-static simulation results of the wide-angle retroreflector for incident angles of $\theta_i = 20°$, 30°,40° in the $\varphi = 0°$ plane at 10 GHz.

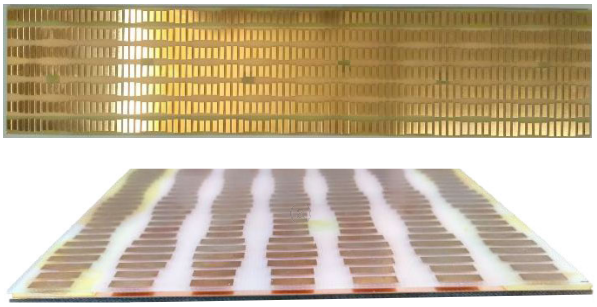

(a)

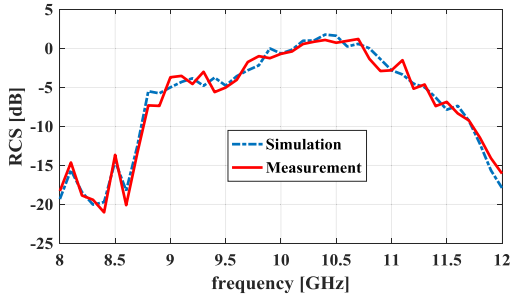

(b)

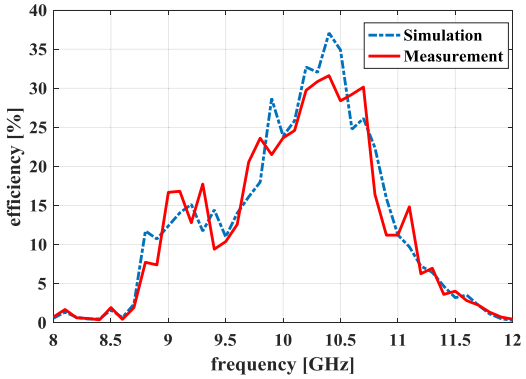

(c)

FIGURE 13. (a) The top and side view of the fabricated wideband retroreflector, (b) and (c) Simulation and measurement results of the proposed retroreflector in the frequency range of 9 GHz ≤ f ≤ 11 GHz.

range of $15° \leq \theta_i \leq 50°$. The calculated efficiency of the fabricated retroreflector, relative to the elevation incident

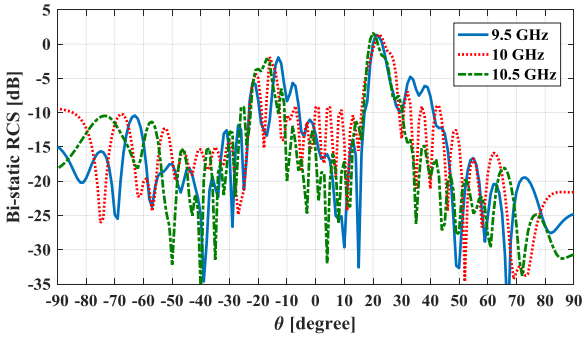

FIGURE 14. The bi-static simulation results of the wideband retroreflector for an incident angle of $\theta_i = 20°$ in the $\varphi = 0°$ plane at three different frequencies.

angle at a frequency of 10 GHz, is depicted in Fig. 11 (d). The minimum efficiency, which occurs within the angular range of $15° \leq \theta_i \leq 50°$, is determined to be 12%. In [20], a quantity called $E(\varphi_i)$ is introduced, representing the average enhancement of the retroreflector's RCS compared to a metal plate with the same dimensions, across a range of elevation incident angles (θ_i) for a specified azimuth incident angle (φ_i). In this case, the obtained value of E is 19.114.

The bi-static simulation results of the wide-angle retroreflector for incident angles of $\theta_i = 20°$, 30°, and 40° in the $\varphi = 0°$ plane at 10 GHz are presented in Fig. 12. This plot illustrates the RCS enhancement around the designed incident angles.

B. WIDEBAND RETROREFLECTOR

The designed wideband retroreflector, intended for the frequency range of 9 GHz ≤ f ≤ 11 GHz with a step size of 0.2 GHz at an incident angle of 20°, has been simulated using CST STUDIO software and subsequently fabricated, as depicted in Fig. 13(a). The measured monostatic RCS of the fabricated retroreflector, along with the calculated efficiency versus frequency, as well as the simulation results at the incident angle of 20° for TE polarization, are shown in Fig. 13(b),(c). It can be observed that the efficiency ranges between 10% and 32%. Furthermore, Figure 14 presents the bi-static simulation results of the wideband retroreflector for an incident angle of $\theta_i = 20°$ in the $\varphi = 0°$ plane at frequencies of 9.5 GHz, 10 GHz, and 10.5 GHz. This plot illustrates the RCS enhancement around the designed incident angle at all three frequencies.

To provide a comprehensive understanding of the characteristics of our work, a comparison between our proposed retroreflector and references [8], [15], [17], [18], [19] is presented in Table 3. It can be observed that while our proposed retroreflector exhibits a higher maximum ripple in the monostatic RCS, it is a single-layer structure with a very small total thickness. This highlights a notable advantage of our design.

V. CONCLUSION

This paper proposes a novel configuration for a metasurface that enables the design of a retroreflector with either

a continuous wide incident angle range (at a single frequency) or a wide frequency range (at a single incident angle). The metasurface is composed of multiple supercells designed with a periodicity gradient to cover the desired wide angular or frequency range. To maximize retroreflectivity at each incident angle or frequency, the supercells contain an equal number of unit cells with a phase gradient property, which are optimized using the array factor method. Two retroreflectors were designed and fabricated based on this metasurface configuration. The first retroreflector provides a continuous wide incident angle range from 15° to 50° at a frequency of 10 GHz. The second retroreflector covers a wide frequency range from 9 GHz to 11 GHz at an incident angle of 20°. The measured results of these retroreflectors demonstrate a minimum efficiency of 12% and 10% within the desired ranges, respectively. Overall, this work presents a novel approach for designing and fabricating retroreflectors with wide incident angle or frequency ranges, showcasing the potential of metasurfaces in achieving versatile retroreflective properties.

REFERENCES

[1] C. Caloz and K. Achouri, *Electromagnetic Metasurfaces: Theory and Applications*. Hoboken, NJ, USA: Wiley, 2021.

[2] S. B. Glybovski, S. A. Tretyakov, P. A. Belov, Y. S. Kivshar, and C. R. Simovski, "Metasurfaces: From microwaves to visible," *Phys. Rep.*, vol. 634, pp. 1–72, May 2016.

[3] S. S. Bukhari, J. Vardaxoglou, and W. Whittow, "A metasurfaces review: Definitions and applications," *Appl. Sci.*, vol. 9, no. 13, p. 2727, Jul. 2019.

[4] C. Tao and T. Itoh, "Nonperiodic metasurfaces for retroreflection of TE/TM and circularly polarized waves," *IEEE Trans. Antennas Propag.*, vol. 68, no. 8, pp. 6193–6203, Aug. 2020.

[5] T. V. Hoang, C.-H. Lee, and J.-H. Lee, "Two-dimensional efficient broadband retrodirective metasurface," *IEEE Trans. Antennas Propag.*, vol. 68, no. 3, pp. 2451–2456, Mar. 2020.

[6] Y. Shang and Z. Shen, "Polarization-independent backscattering enhancement of cylinders based on conformal gradient metasurfaces," *IEEE Trans. Antennas Propag.*, vol. 65, no. 5, pp. 2386–2396, May 2017.

[7] Y. Jia, J. Wang, Y. Li, Y. Pang, J. Yang, Y. Fan, M. Feng, and S. Qu, "Enhancing backward scattering using metasurfaces," in *Proc. Int. Conf. Microw. Millim. Wave Technol. (ICMMT)*, May 2018, pp. 1–3.

[8] M. Feng, Y. Li, J. Zhang, Y. Han, J. Wang, H. Ma, and S. Qu, "Wide-angle flat metasurface corner reflector," *Appl. Phys. Lett.*, vol. 113, no. 14, 2018, Art. no. 143504.

[9] E. Doumanis, G. Goussetis, G. Papageorgiou, V. Fusco, R. Cahill, and D. Linton, "Design of engineered reflectors for radar cross section modification," *IEEE Trans. Antennas Propag.*, vol. 61, no. 1, pp. 232–239, Jan. 2013.

[10] Y. Jia, J. Wang, Y. Li, Y. Pang, J. Yang, Y. Fan, and S. Qu, "Retro-reflective metasurfaces for backscattering enhancement under oblique incidence," *AIP Adv.*, vol. 7, no. 10, Oct. 2017, Art. no. 105315.

[11] A. M. H. Wong, P. Christian, and G. V. Eleftheriades, "Binary Huygens' metasurfaces: Experimental demonstration of simple and efficient near-grazing retroreflectors for TE and TM polarizations," *IEEE Trans. Antennas Propag.*, vol. 66, no. 6, pp. 2892–2903, Jun. 2018.

[12] V. S. Asadchy, A. Díaz-Rubio, S. N. Tcvetkova, D.-H. Kwon, A. Elsakka, M. Albooyeh, and S. A. Tretyakov, "Flat engineered multichannel reflectors," *Phys. Rev. X*, vol. 7, no. 3, Sep. 2017, Art. no. 031046.

[13] M. Kalaagi and D. Seetharamdoo, "Retrodirective metasurfaces from non-reciprocal to reciprocal using impedance modulation for high-super-cell-periodicity designs," *Appl. Phys. A, Solids Surf.*, vol. 126, no. 4, pp. 1–7, 2020.

[14] M. Memarian, X. Li, Y. Morimoto, and T. Itoh, "Wide-band/angle blazed surfaces using multiple coupled blazing resonances," *Sci. Rep.*, vol. 7, no. 1, pp. 1–12, Feb. 2017.

[15] A. Arbabi, E. Arbabi, Y. Horie, S. M. Kamali, and A. Faraon, "Planar metasurface retroreflector," *Nature Photon.*, vol. 11, no. 7, pp. 415–420, Jul. 2017.

[16] G. Y. Song, Q. Cheng, T. J. Cui, and Y. Jing, "Acoustic planar surface retroreflector," *Phys. Rev. Mater.*, vol. 2, no. 6, Jun. 2018, Art. no. 065201.

[17] A. Pesarakloo and M. Khalaj-amirhosseini, "Planar, wide-band omnidirectional retroreflector using metal-only transmitarray structure for TE and TM polarizations," *Sci. Rep.*, vol. 12, no. 1, pp. 1–12, Jul. 2022.

[18] A. Pesarakloo and M. Khalaj-Amirhosseini, "Planar metal-only omnidirectional retroreflector using transmitarray and blazed grating for TE and TM polarizations," *Opt. Exp.*, vol. 30, no. 15, pp. 28121–28141, 2022.

[19] Y.-Q. Liu, S. Li, J. Guo, L. Li, and H. Yin, "Planar microwave retroreflector based on transmissive gradient index metasurface," *New J. Phys.*, vol. 22, no. 6, Jun. 2020, Art. no. 063044.

[20] A. Pesarakloo and M. Khalaj-Amirhosseini, "Wide-angle monostatic RCS enhancement using symmetrical periodic structures," *J. Electromagn. Waves Appl.*, vol. 35, no. 15, pp. 1987–2000, Oct. 2021.

ALI PESARAKLOO received the B.S. degree in electrical engineering from the Babol Noshirvani University of Technology (NIT), Iran, in 2011, and the M.Sc. degree in telecommunications engineering from the Iran University of Science and Technology, Iran, in 2015. He is currently pursuing the Ph.D. degree in electromagnetic fields and waves with the Department of Electrical Engineering, Iran University of Science and Technology (IUST), Tehran, Iran.

His research interests include electromagnetics, array antenna, metasurfaces, and active circuits.

MOHAMMAD KHALAJ-AMIRHOSSEINI was born in Tehran, Iran, in 1969. He received the B.Sc., M.Sc., and Ph.D. degrees in electrical engineering from the Iran University of Science and Technology (IUST), Tehran, in 1992, 1994, and 1998, respectively. He is currently a Professor with the School of Electrical Engineering, IUST. His current research interests include electromagnetics, microwaves, antennas, radio wave propagation, and electromagnetic compatibility.